Quantifying anisotropic thermal transport in two-dimensional perovskite (PEA$_2$PbI$_4$) through cross-sectional scanning thermal microscopy

Abhishek Maiti [1,2,*] Khushboo Agarwal,[1] Sergio Gonzalez-Munoz [1] and Oleg. V. Kolosov[1,3,†]

[1]*Physics Department, Lancaster University, Lancaster LA14YB, United Kingdom*
[2]*School of Physical Sciences, Indian Association for the Cultivation of Science, Jadavpur, Kolkata 700032, India*
[3]*Material Science Institute, Lancaster University, Lancaster LA14YB, United Kingdom*

In this paper, we investigated the anisotropic thermal transport in two-dimensional (2D) perovskite (phenethylammonium lead iodide) nanolayers through a measurement technique called cross-sectional scanning thermal microscopy. In this method, a target perovskite layer on a substrate was oblique polished with an Ar ion beam to create a low-angle wedge with nanoscale roughness that is followed by high-vacuum scanning thermal microscopy to obtain the thermal conductance map as a function of local thickness. The experimentally obtained data were processed with an analytical model and validated by the finite elemental analysis simulation to quantify the in-plane ($k_{l,xy}$) and cross-plane thermal conductivities ($k_{l,z}$) of the 2D perovskite from a single set of measurements with nanoscale resolution. We obtained ultralow thermal conductivity ($k_l = 0.25 \pm 0.05 \, \text{W m}^{-1} \, \text{K}^{-1}$) for the 2D perovskite along with an anisotropy ($k_{l,xy} = 0.45 \pm 0.05 \, \text{W m}^{-1} \, \text{K}^{-1}$ and $k_{l,z} = 0.13 \pm 0.05 \, \text{W m}^{-1} \, \text{K}^{-1}$) linked to the unique structure of the perovskite and different phonon lifetimes and group velocities for in-plane and out-of-plane directions. The results that are available are essential for the thermal management of 2D perovskite-based optoelectronic devices and potential thermoelectric applications of these materials.

I. INTRODUCTION

In recent years, Ruddlesden-Popper (RP) hybrid halide perovskites have gained widespread attention as an emerging class of two-dimensional (2D) materials owing to their electronic and photophysical properties [1–4]. This class of quantum well-like materials exhibiting excellent light-emitting and optoelectronic properties is considered an alternative to their three-dimensional (3D) counterparts [5]. The excellent performance of the compound in solar cells, photodetectors, and light-emitting diodes has been ascribed to many exceptional properties, such as solution processability [6], band gap tunability [7], high extinction coefficient [8], high photoluminescence (PL) quantum yield [9], excitonic effects [1,10], and improved ambient stability [11]. While the photophysics and carrier dynamics have been intensively studied [12,13], a much less explored aspect of this exciting class of materials is their thermal properties. A fundamental understanding of different thermal parameters and phonon transport is essential for the proper thermal management of 2D perovskite-based existing devices [14], potential thermoelectric applications of these materials [15,16], and development of advanced photovoltaic devices based on the hot phonon bottleneck effect [17].

In this direction, conventional methods were employed to measure the thermal conductivity of different 3D and 2D perovskites [18–24]. An ultralow thermal conductivity

$(0.3 - 0.5 \, \text{W m}^{-1} \, \text{K}^{-1})$ was obtained for the 3D perovskite through the 3ω-method, frequency or time domain thermoreflectance, time-resolved vibrational-pump–visible-probe spectroscopy, and so forth [21–24]. On the other hand, the 2D perovskites also exhibit a low thermal conductivity; however, due to the anisotropic layered structure, it was found to be anisotropic in nature. As a result, different sets of measurements were required to measure the in-plane (transient thermal grating, time domain thermoreflectance) and out-of-plane (frequency domain thermoreflectance, thermal diffusivity) contributions of the thermal conductivity tensor [19,20,25,26]. Despite these reports on ultralow thermal conductivity (k_l) and the underlying phonon transport mechanism, a complete understanding of heat dissipation in 2D perovskite layers remains ambiguous due to the limitations of existing thermal characterization techniques. As such, the prevailing macroscopic measurement methods are not appropriate for these compounds, especially in their thin-film form where ballistic heat transport and phonon scattering at the interfaces significantly influence the diffusive heat flow [27]. In this regard, nondestructive scanning thermal microscopy (SThM) approaches may open a route to determine local thermal properties of 2D perovskite thin films overcoming the limitations of classical thermal characterization techniques [28–30]. Moreover, it would be more intriguing to develop a method for the measurement of both in-plane ($k_{l,xy}$) and out-of-plane ($k_{l,z}$) components of thermal conductivity simultaneously from a single set of measurements to minimize the systematic error of the existing methods.

In this paper, we measured k_l of an archetypal 2D perovskite named phenethylammonium lead iodide

*abhishek.juphysics@gmail.com
†o.kolosov@lancaster.ac.uk

[(PEA)$_2$PbI$_4$] through a unique tool called cross-sectional SThM (xSThM). This microscopic technique is not only capable of the qualitative thermal imaging of the perovskite with the nanoscale resolution to map the local thermal conductance but also holds the unprecedented opportunity to provide absolute quantitative values of $k_{l,xy}$ and $k_{l,z}$ components of thermal conductivity via a matched analytical model. In this method, a low-angle wedge cut in the perovskite thin film (on a Si/SiO$_2$ substrate) was formed through beam exit cross-sectional polishing (BEXP) followed by a high-vacuum SThM investigation [31]. As a result, SThM in one map obtains the dependence of the thermal resistance as a function of thickness t, replacing the need to create and measure a set of samples of different thicknesses. The quantitative values of both $k_{l,xy}$ and $k_{l,z}$ are then obtained along with interfacial thermal resistance (r_{int}) once the experimental data were compared with an appropriate analytical Muzychka-Spièce model that was independently validated via finite elemental analysis (FEA) simulation [32–34]. To be specific, the measured values of $k_{l,xy}$ and $k_{l,z}$ in the material were $0.45 \pm 0.05\,\mathrm{W\,m^{-1}\,K^{-1}}$ and $0.13 \pm 0.05\,\mathrm{W\,m^{-1}\,K^{-1}}$, respectively. Our results also reveal the existence of thermal anisotropy ($k_{l,xy}/k_{l,z} \sim 3.4$) in the compound that originates in the differences between (in-plane) heat conduction in the continuous inorganic layer vs the out-of-plane heat transport interrupted at the organic-inorganic interfaces. In this paper, we provide a generic technique to measure the quantitative ultralow value of average thermal conductivity k_l in 2D materials as well as its deconvolution into anisotropic thermal conductivity components $k_{l,xy}$ and $k_{l,z}$ using a single set of measurements. Moreover, this paper is beneficial for development of the thermal management strategies for 2D perovskite-based optoelectronic devices and their possible thermoelectric applications.

II. MATERIALS AND METHODS

A. Materials

Phenethylammonium iodide (PEAI, 99%), lead iodide (PbI$_2$, 99%), and anhydrous N, N-dimethyl formamide (DMF, 99.8%) were purchased from Sigma-Aldrich chemical company. All the materials were kept inside a nitrogen-filled glovebox with well-maintained oxygen and moisture levels < 0.1 ppm and used without further purification.

B. Fabrication and characterization of the thin films

For the fabrication of (PEA)$_2$PbI$_4$ thin films, a precursor solution was prepared by dissolving PEAI (2 M) and PbI$_2$ (1 M) into DMF solvent. The mixture was stirred continuously at 70 °C to form a clear and homogeneous solution. After that, glass and SiO$_2$-coated Si substrates (Si/SiO$_2$) were cleaned following a usual protocol with ethanol, acetone, and isopropyl alcohol for 15 min each in a bath sonicator (37 kHz), followed by plasma cleaning to remove organic residues. Finally, the precursor solution was spun at 2500 rpm for 30 s followed by annealing of the film at 80 °C for 15 min. The perovskite films were characterized through conventional techniques such as x-ray diffraction (XRD), optical absorbance, and PL spectroscopy to ensure their phase purity.

Such measurements were carried out in a Rigaku Smart Lab x-ray diffractometer (Cu $K\alpha$ radiation = 1.5406 Å), Shimadzu UV-vis spectrophotometer, and Horiba Jobin Yvon spectrofluorometer (excitation at 405 nm), respectively.

C. BEXP

To obtain an ultralow wedgelike cut in the sample (2D perovskite on Si/SiO$_2$ substrate), we used the BEXP technique carried out in an EM TIC 3X triple ion beam cutter system (Leica Microsystems). In this technique (Fig. S1(a) in the Supplemental Material [35]), the sample was placed on a tilted (5°) stage to the horizontal plane. A shade mask was used in front of the stage so that the cut could be executed on the exposed material by intersecting coplanar argon (Ar) beams coming from three guns. The entire process was executed in a high vacuum (10^{-5} Torr) through different steps such as warmup of the guns (1 kV, 1 mA, and 15 min), prepolishing (5 kV, 2 mA, and 15 min), nanocutting or polishing (7 kV, 2.6 mA, and 7 h), and postpolishing (1 kV, 1 mA, and 1 h). This technique is called BEXP as the beam exits at a glancing angle to the sample surface to produce the cut with near-atomic roughness and negligible surface damage [36].

D. SThM

The cross-sectioned 2D perovskite film was then transferred to the high-vacuum chamber for SThM measurements that could image the thermal response with a high spatial resolution (~ 50 nm) in contrast to the far-field optical techniques [34,37]. It may be noted that a high vacuum is desirable to avoid additional heat transfer through air and the formation of water meniscuses at the tip apex [38–40]. The experiments were carried out in a Smena (NT-MDT Spectrum) scanning probe microscope with custom-built SThM electronics. In this system, the thermal probe was composed of a Si$_3$N$_4$ cantilever with a palladium (Pd) film deposited on it through thermal evaporation. The spring constant of the tip was $0.4\,\mathrm{N\,m^{-1}}$ spring constant with <100 nm tip radius. The probe used a thermal resistive heater and could sense the variations in temperature during the scan over the material [40,41]. At a more technical detailed level (Fig. S1(b) in the Supplemental Material [35]), the thermal probe was a resistor with electrical resistance R_{probe} in a Wheatstone bridge circuit with two known resistors (R_1 and R_2) and a variable resistor R_3. The SThM probe is used as a local heater of the 2D perovskite with the consideration that the heat source is concentrated near the extreme point of the tip apex. When the probe is energized via DC and AC voltage and brought into close contact with the perovskite surface, a heat flow is generated from the tip to the sample due to a temperature gradient. This changes the temperature of the probe and hence the resistance of the probe which is monitored as the change of output voltage of the Wheatstone bridge [37]. The experimental data were fitted with an analytical model in MATLAB software. In addition, FEA simulation was carried out in COMSOL Multiphysics 5.6 software to validate the experimental results.
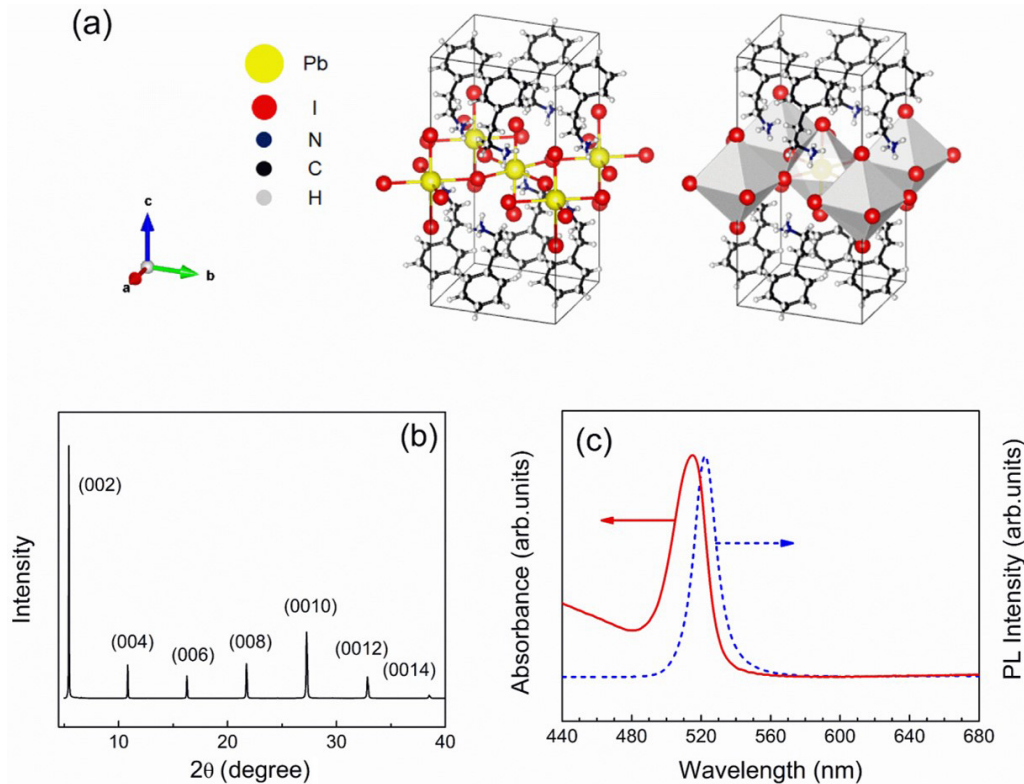
FIG. 1. (a) Schematic representations of $(PEA)_2PbI_4$ crystal structure. The first one shows the ball-stick model of the crystal. In the second polyhedral model, the octahedra are presented. (b) and (c) X-ray diffraction (XRD) patterns, optical absorbance, and photoluminescence spectra of the $(PEA)_2PbI_4$ thin film.

III. RESULTS AND DISCUSSIONS

A. Characterization of 2D perovskite

The crystal structure of $(PEA)_2PbI_4$ perovskite reveals that it is formed with alternatively stacking of organic spacer layers and the inorganic octahedral slabs [repetition of the structure as shown in Fig. 1(a)]. It may be noted that, due to the large size of the bulky spacer cation $(PEA)^+$, it could not be tolerated in between the cages of inorganic octahedrons ($[PbI_4]^{2-}$), resulting in a formation of insulating spacer layer depending on intermolecular forces. The large spacer chains are aligned in the out-of-plane direction having covalent bonds (C-C and C-N). In addition, weak van der Waals and electrostatic interactions could be observed between two vertically stacked organic chains and at the organic-inorganic interfaces. On the other hand, there are strong ionic bonds in the in-plane direction originating from the continuous $[PbI_4]^{2-}$ octahedral framework [20,42,43].

To confirm the phase purity of the thin film, we have presented the XRD pattern in Fig. 1(b). The diffraction pattern is indexed according to the previous report and suggests the evolution of strong $(002l)$ reflection series [44]. Such an XRD pattern indicates the formation of the film with layers oriented parallel to the substrate preferred along the $\langle 001 \rangle$ direction [43]. In addition, the optical absorbance and PL spectra of the as-prepared film are presented in Fig. 1(c), showing a characteristic band gap of the material ~ 2.2 eV, typical narrow exciton absorption, and emission lines, with a small Stokes

shift [45]. Such results confirmed the phase pure formation of the material before proceeding to further measurements.

B. xSThM

After ensuring the purity of the 2D perovskite phase, we proceeded toward the cross-sectioning of the film (fabricated on a Si/SiO_2 substrate) through the BEXP method followed by SThM investigation as described previously. As the entire sample system is composed of an assembly of different materials (Si, SiO_2, and 2D perovskite), the obtained wedge cut provides a perfect platform that includes three different regions and interfaces and can be studied in a single measurement as a function of tip position during SThM characterization. In Fig. 2(a), the 3D topography of the cross-sectional surface is presented. It is difficult to identify different materials and interfaces from the topography image due to the near-perfect nano-cross-sectioning via BEXP. On the contrary, the deflection and thermal images allow good differentiation of these different layers [Figs. 2(b) and 2(c)]. The extracted data [Fig. 2(d)] revealed the height profile (Z-height) of the layers (SiO_2 and 2D perovskite) as a function of tip position x along the section. Due to the dissimilar properties of Si, SiO_2, and perovskite, a different milling rate is also expected with the Ar beams, which due to the low angle incidence results in an observable but minor change of angle at the interfaces. This change is useful to identify different interfaces of the entire sample system. In addition,
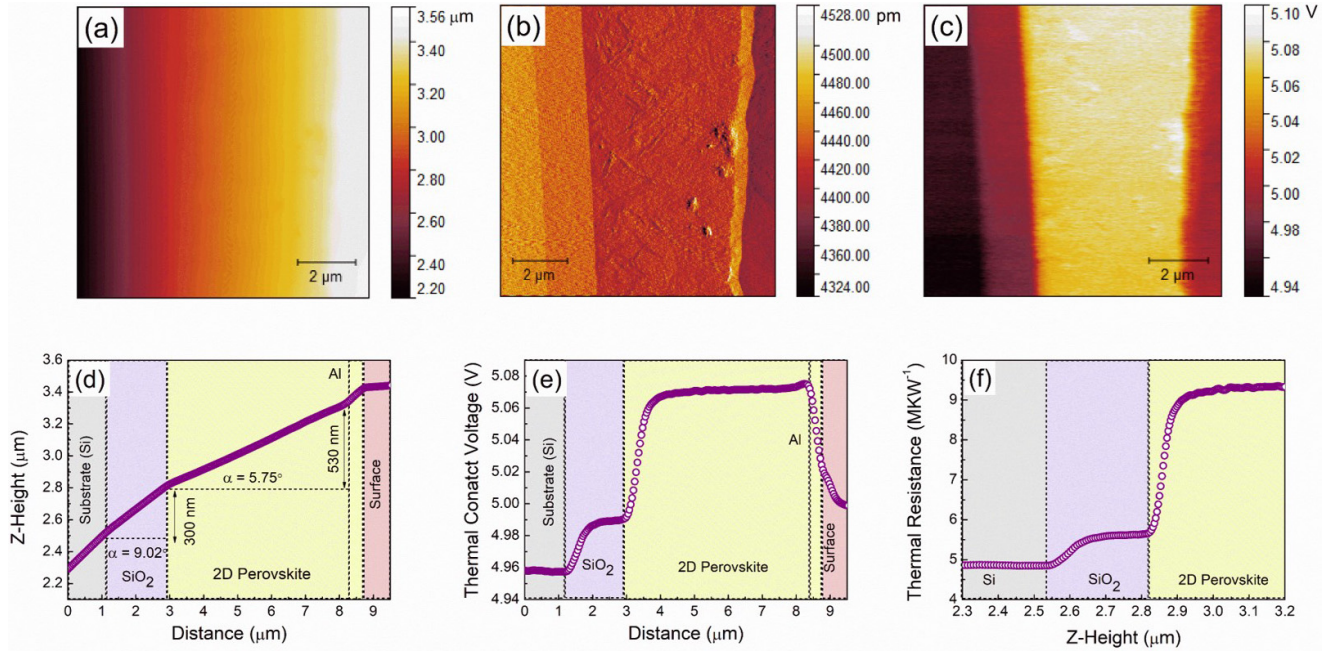
FIG. 2. (a) Topography, (b) deflection, (c) thermal signal image, (d) section analysis, (e) thermal voltage, and (f) variation of thermal resistance at different regions of the beam exit cross-sectional polishing (BEXP) cut sample as mentioned in the plots.

a very thin layer of aluminum (Al) was observed at the top of the 2D perovskite layer which could be formed during the BEXP cut when the Ar beams exit from the cut sample (see Supplemental Material [35]). At the same time, due to the calibration of the scanner, the thickness of the layer is directly measured as a function of the lateral position, as described elsewhere, with subnanometer precision [31].

Now during scanning when the tip moves over the wedge cut, contact thermal voltage (V_c) could be obtained as a function of t simultaneously along with the topography as well as throughout the cut defined as $V_c(t)$; this thermal signal profile is presented in Fig. 2(e). The raw thermal results showed a different voltage contrast of the Si, SiO$_2$, and 2D perovskite layers due to the different thermal properties of each material. The thermal resistances of different regions over the cut were derived as a function of t as follows [46]:

$$R_x(t) = C_{\text{corr}} \frac{V_c(t)}{V_{nc} - V_c(t)} R_P, \tag{1}$$

where R_P represents the probe thermal resistance at high vacuum (2.38×10^5 K W^{-1}) that was obtained through a calibration [47], and C_{corr} represents a correction factor that accounts for the deviation of the approximation that the heat source is concentrated only at the extreme point of the tip apex due to tip geometry [47]. The value of V_{nc} for the tip out of the contact with the sample is obtained by doing an approach-and-retract thermal scan over the cut and averaging them. In Fig. 2(f), we have presented variation of $R_x(t)$ at different regions and interfaces through the wedge cut. First, we observed stable thermal resistance of Si followed by a clear increase at SiO$_2$ due to a much higher thermal conductivity of Si (135 W m^{-1} K^{-1}) than SiO$_2$ (1.4 W m^{-1} K^{-1}) [48,49]. Similarly, the 2D perovskite showed a higher thermal resistance than SiO$_2$ and finally reached a quasiconstant nature at

higher thickness. In addition, we witnessed a sudden jump of $R_x(t)$ at the SiO$_2$–perovskite interface, suggesting a high interfacial thermal resistance at the SiO$_2$–perovskite interface. Although these preliminary observations are consistent with the existing literature regarding the ultralow thermal conductivity of 2D perovskite [18–20], it is not enough for the quantitative analysis that has been undertaken below.

C. Analytical model for SThM response to study the anisotropic material

For the quantitative estimation of thermal conductivity in a 2D perovskite, we used an analytical model that describes heat spreading within the layer on a substrate, as mentioned elsewhere [32,33]. It may be recalled that the 2D perovskite film was fabricated on a Si substrate having a SiO$_2$ layer. Hence, the entire system could be represented as a combination of two different heterojunctions (Si/SiO$_2$ and SiO$_2$/2D perovskite) and demonstrated as a layer (top material) with thermal conductivity k_l on a uniform substrate (bottom material) having a thermal conductivity k_s. As mentioned earlier, the wedge cut allows us to carry out SThM measurements as a function of t in a single measurement as effective thickness of the layer under the probe is changed depending on the position of the tip (Fig. S2 in the Supplemental Material [35]).

To quantify the thermal properties through this analytical model, we have expressed the total thermal resistance of the tip-sample system [Fig. 2(f)] as a combination of two components connected in series as $R_x(t) = R_s(t) + R_c$, where R_s represents the total spreading thermal resistance of the sample, and R_c denotes the contact thermal resistance between the tip and sample [34]. As the experiments were carried out in vacuum, the contribution of water meniscus conductance has been eliminated [39], and we could consider that R_c is constant and solely governed by the solid-solid contact thermal

resistance depending on the contact radius (a) and the thermophysical properties of the scanned material [30]. Although R_c is independent of the tip position during scanning, it has a nonzero contribution that should be eliminated, as the analytical model describes only the heat spreading within the layer on a substrate [32,33]. In addition, for both heterostructures, at the interfaces, the tip-sample contact could be occurring simultaneously, touching both materials, resulting in a sudden jump of thermal resistance at the transition point(s), leading to artifacts during fitting. To eliminate this, only the data at a distance away from the transition point by the contact radius were used, with t_l denoting the thickness of each consecutive point starting from the point $t_l = t_0$. To exclude the unknown value of the tip-sample contact resistance R_c, the difference between the thermal resistances at thicknesses t_l and t_0 was used as follows:

$$R_l(t_l) = R_x(t_l) - R_x(0) = R_s(t_l) + R_c - R_s(0) - R_c$$
$$= R_s(t_l) - R_s(0), \tag{2}$$

where $R_x(0)$ represents the initial spreading resistance at $t_0 \to 0$ nm of thickness, and $R_l(t_l)$ denotes the difference in the spreading resistance at each consecutive thickness point above t_0 and the thermal resistance at the point t_0. Then the final experimental data for both the nanostructure could be interpreted as R_l as a function of t_l, which is compatible for fitting to the isotropic heat spreading model for $R_l(t_l)$ described by Muzychka and Spièce [32–34]:

$$R_l(t_l) = \frac{1}{\pi k_l a} \int_0^\infty \left\{ \frac{1 + K \exp\left[-\left(\frac{2x t_{\text{eff}}}{a}\right)\right]}{1 - K \exp\left[-\left(\frac{2x t_{\text{eff}}}{a}\right)\right]} \right\} J_1(x) \sin(x) \frac{dx}{x^2}, \tag{3}$$

where k_l represents the top layer isotropic thermal conductivity, and J_1 corresponds to the first-order Bessel function. In addition, K and t_{eff} are defined as

$$K = \frac{1 - \frac{k_l}{k_s}}{1 + \frac{k_l}{k_s}} \quad \text{and} \quad t_{\text{eff}} = t_l + r_{\text{int}} k_l, \tag{4}$$

and k_s represents the thermal conductivity of the substrate, r_{int} denotes the layer-substrate interfacial thermal resistance, and t_l is the thickness of each layer. While this model is appropriate when the top layers exhibit inherent isotropic thermal transport, for an anisotropic transport of the top layer, it is possible to modify these formulae by transforming t_l and k_l as in the following [32,33]:

$$t_{l,\text{anis}} = \frac{t_l}{\sqrt{\frac{k_{l,z}}{k_{l,xy}}}} \quad \text{and} \quad k_{l,\text{anis}} = \sqrt{k_{l,xy} k_{l,z}}. \tag{5}$$

D. Quantitative analysis of thermal conductivity: Fitting results and FEA simulation

To obtain average thermal conductivity $k_{l,\text{anis}}$ of the 2D perovskite layer using the abovementioned model, we applied a two-step fitting due to the need to find several independent parameters [Eqs. (3)–(5)] such as a, C_{corr}, $k_{l,xy}$, $k_{l,z}$, and r_{int}. In the first step, the analytical fitting was carried out in the Si/SiO$_2$ heterostructure considering it as a reference with known values of k_s (k_{Si}) and k_l (k_{SiO_2}) to obtain a and C_{corr} as

fitting parameters. In the next step, these values were served as known inputs when the model was applied to the SiO$_2$/2D perovskite heterostructure to obtain k_l ($k_{l,\text{anis}}$, $k_{l,xy}$, $k_{l,z}$) of 2D perovskite and r_{int} between SiO$_2$ and 2D perovskite. In addition, we have validated our fitting results with FEA simulation which is also helpful to qualitatively understand the thermal properties of the system in terms of temperature distribution and heat flow directions.

1. Isotropic model fitting for Si/SiO$_2$ *heterojunction*

According to previous studies, SiO$_2$ on a Si substrate exhibits isotropic thermal transport [34,48]. Hence, introducing $k_s = 130\,\text{W}\,\text{m}^{-1}\,\text{K}^{-1}$ and $k_l = 1.4\,\text{W}\,\text{m}^{-1}\,\text{K}^{-1}$ as known parameters during the first fitting [48–50], we could extract a and C_{corr} along with r_{int} as fitting parameters by applying the isotropic model [Eqs. (3) and (4)]. However, before proceeding to the actual refinement of the experimental data, it would be intriguing to understand how each of these fitting parameters governs the overall thermal spreading resistance analytically and theoretically (Fig. S3 in the Supplemental Material [35]). Using this approach, a desired goodness of fit was achieved [Fig. 3(a) and Table I]. We extracted $a = 55.4 \pm 0.2$ nm from the fitting which is in good agreement with the specification of the probe with the tip radius <100 nm. Similarly, we obtained a reasonable value of $C_{\text{corr}} = 5.15$; in an ideal case, this should be unity, suggesting that the heat source is concentrated only at the extreme point of the tip apex [47]. Moreover, the interfacial thermal resistance between Si and SiO$_2$ ($r_{\text{Si–SiO}_2}$) was found to be $\sim 10^{-11}\,\text{K}\,\text{m}^2\,\text{W}^{-1}$. While this value is much smaller than the previously reported value of $10^{-9}\,\text{K}\,\text{m}^2\,\text{W}^{-1}$ [34], our analysis (see the forward curves in Fig. S3 in the Supplemental Material [35]) inferred that the influence of interfacial thermal resistance on the thermal transport in such a system is negligible in the range of 10^{-9} to $10^{-11}\,\text{K}\,\text{m}^2\,\text{W}^{-1}$; in this range, these curves overlap with each other over the entire thickness region. Given a wide range of values that satisfy our fitting, these data do not contradict the literature values. This means that, first, our measurements mainly provide the upper range of the thermal resistance and, significantly, that sample-substrate interfacial thermal resistance does not affect the absolute values of the layer thermal conductivity and its anisotropy—the key parameters of interest in this paper.

These obtained fitting parameters were also introduced in a realistic model in the COMSOL interface to obtain the idea of thermal transport in this system. A planar mode was used for an optimized simulation experience analogous to a real device system, and given the extreme similarity with the wedge model (Fig. S4 in the Supplemental Material [35]), we can argue that the results extracted from the plane model are highly reliable and descriptive. In this direction, we mainly proceeded to understand the temperature distribution (color gradient) and heat flow direction (streamlines) in the YZ direction. As such, we depicted the thermal behavior at two different tip positions indicating two different thicknesses (thick and thin layers). At a higher thickness, a higher temperature gradient and an isotropic heat flow were observed [Fig. 3(b)]. On the other hand, at a lower thickness (Fig. S5 in the Supplemental Material [35]), the temperature gradient
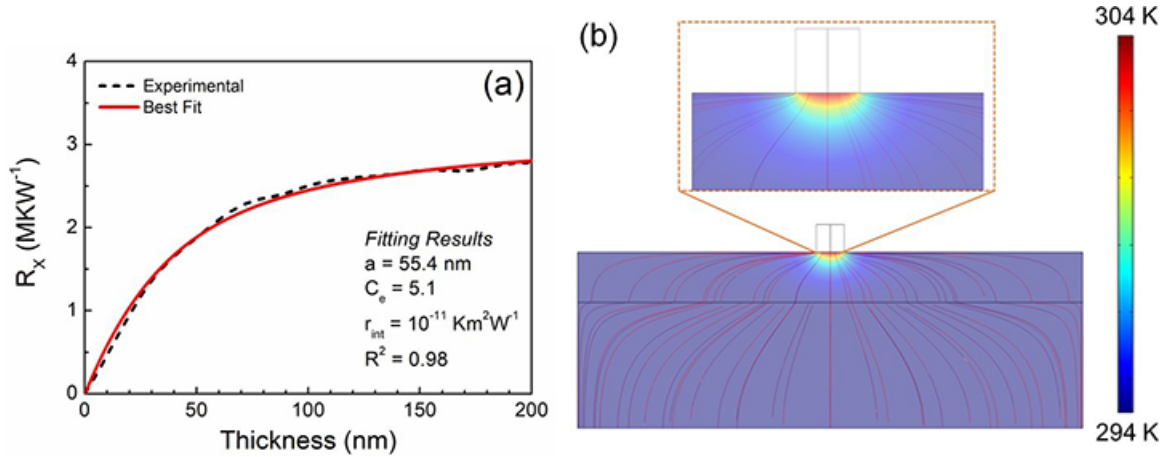
FIG. 3. (a) The fitting plot for the Si/SiO$_2$ heterojunction (analytical model). (b) Finite elemental analysis (FEA)-simulated results of thermal gradient and heat flow at a high thickness (the inset shows a zoomed-in view).

was found to be very localized under the tip and did not influence its surroundings, creating only a minor temperature difference. Under this situation, mainly r_{Si-SiO_2} restricts the heat transport toward Si, resulting in a small thermal gradient.

2. Anisotropic model fitting for SiO$_2$/2D perovskite heterojunction

After obtaining some of the common parameters from the previous analysis, we could finally use the Muzychka-Spièce model of heat spreading [Eq. (5)] for the second heterojunction considering SiO$_2$ as a substrate and the 2D perovskite as a top layer to determine its average thermal conductivity ($k_{l,anis}$ or k_{avg}). Due to the anisotropic layered structure, such 2D perovskites are expected to exhibit anisotropic thermal transport [20]; hence, the anisotropic model was considered instead of the isotropic one [Eq. (3)]. Although we considered Si/SiO$_2$ and SiO$_2$/2D perovskite as two different heterojunctions during this analytical method, no significant change was expected for a and C_e as all three materials (Si/SiO$_2$/2D perovskite) were thermally imaged sequentially as a single system under the same SThM probe and similar geometrical configuration. Hence, the previously determined values of $a = 55.4$ nm and $C_{corr} = 5.15$ along with $k_s = 1.4$ W m^{-1} K^{-1} were used as known inputs during the fitting to obtain $k_{l,\,anis}$ (k_{avg}) = $\sqrt{k_{l,xy}k_{l,z}}$, $\Delta_{anis} = \frac{k_{l,xy}}{k_{l,z}}$, and interfacial thermal resistance be-

tween SiO$_2$ and 2D perovskite ($r_{int_{SiO_2-Perovskite}}$), respectively, as fitting parameters and to deconvolute them into $k_{l,xy}$ and $k_{l,z}$ finally. However, like the Si/SiO$_2$ heterojunction, we first generated a series of simulated curves for different $k_{l,\,anis}$ (k_{avg}) and Δ_{anis} to get a preliminary idea about these parameters before the original fitting [Figs. 4(a), 4(b), 4(d), and 4(e)]. To start with, by comparing the experimental data and the forward curves, the value of $k_{l,\,anis}$ (k_{avg}) of the top 2D perovskite layer can be reasonably well estimated to be ~ 0.25 W m^{-1} K^{-1} [Fig. 4(a)]. On the other hand, visual curve comparison appears to be less sensitive to the anisotropy ratio; for example, it looks like different curves ($\Delta_{anis} = 3$, 5, and 10) lie close to each other [Fig. 4(b)]. However, a close inspection reflects that these theoretical curves are closer at a high thickness and become quasiconstant to overlap with each other. Hence, it is predominantly the transition region [Fig. 2(f)] vis-à-vis the initial slope [Fig. 4(b)] that reflects the anisotropic behavior of the heat transport. Based on the similarity of the initial slope, we could conclude that the experimental curve lies between 3 and 5 [inset Fig. 4(b)], to be specifically closer to a value of 3, with some amount of error. In this direction, we refined these results through an iterative method to obtain much smaller error for both average heat conductivity $k_{l,\,anis}$ (k_{avg}) = 0.25 ± 0.05 W m^{-1} K^{-1} and, essentially, anisotropy ratio $\Delta_{anis} = 3.4 \pm 0.3$ [Fig. 4(c)].

TABLE I. Fitting parameters as obtained from the analytical model (Muzychka-Spièce formulation) when experimental data is fitted to Eqs. (3)–(5).

Fitting parameters	Si/SiO$_2$		SiO$_2$/perovskite	
	Substrate Si	Top layer SiO$_2$	Substrate SiO$_2$	Top layer (PEA)$_2$PbI$_4$
Contact radius, a (nm)		55.0		
Interfacial thermal resistance, r_{int} (10^{-11} Km^2 W^{-1})		1.99	100	
Correction factor, C_e	5.15	5.15	5.15	5.15
Average thermal conductivity of substrate, k_s (W m^{-1} K^{-1})	130.0	—	1.4	—
Average thermal conductivity of top layer, k_l (W m^{-1} K^{-1})	—	1.4	1.4	0.25
In-plane thermal conductivity of top layer, $k_{l,xy}$ (W m^{-1} K^{-1})	—	1.4	—	0.45
Out-of-plane plane thermal conductivity of top layer, $k_{l,z}$ (W m^{-1} K^{-1})	—	1.4	—	0.13
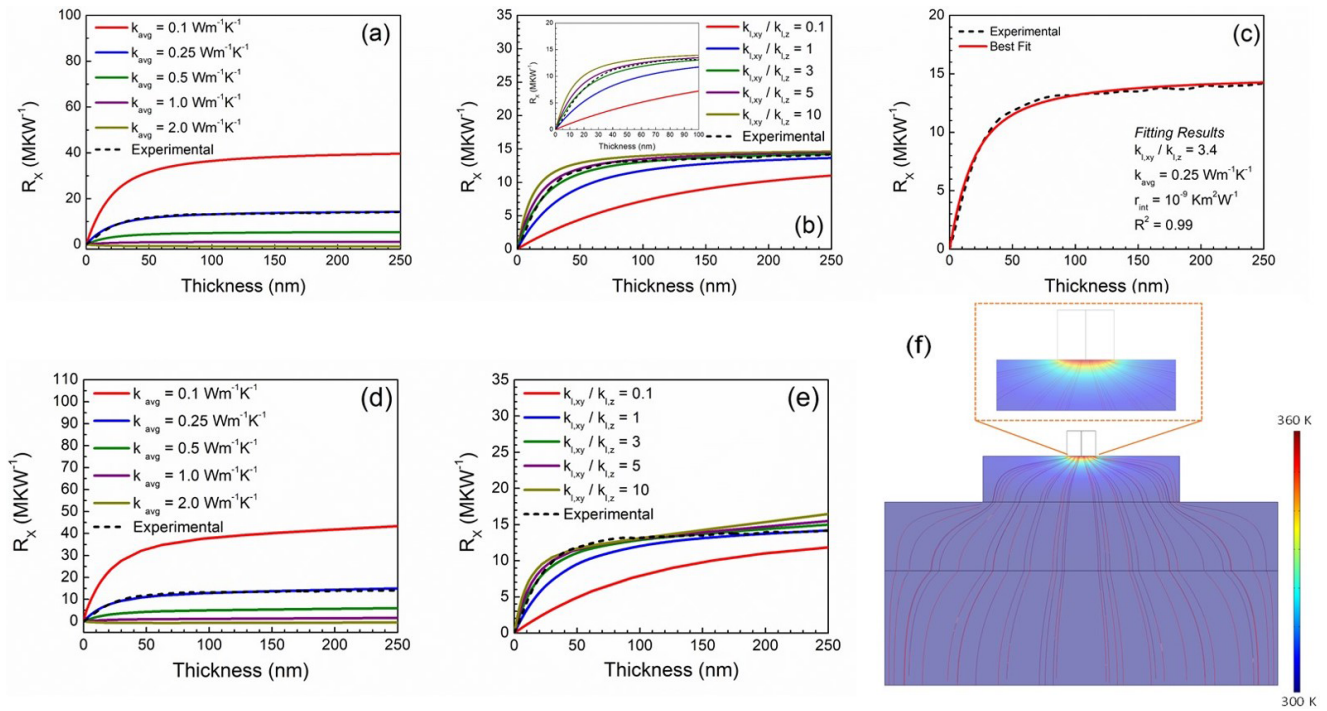
FIG. 4. (a) and (b) Simulated thermal resistance dependence for different $k_{l,\,\text{anis}}$ (k_{avg}) and Δ_{anis} ($\frac{k_{l,xy}}{k_{l,z}}$) and (c) the fitting plots for the Si/SiO$_2$ heterojunction (analytical model). (d) and (e) Finite elemental analysis (FEA)-simulated forward plots for different $k_{l,\,\text{anis}}$ (k_{avg}) and Δ_{anis}. ($\frac{k_{l,xy}}{k_{l,z}}$). (f) FEA-simulated results of thermal gradient and heat flow (inset shows a zoomed-in view).

The errors in this case are directly provided by several measurements followed by statistical analysis. These values, in turn, result in the in-plane and/or out-of-plane values of the thermal conductivity of $k_{l,xy} = 0.45 \pm 0.05 \,\text{W}\,\text{m}^{-1}\,\text{K}^{-1}$ and $k_{l,z} = 0.13 \pm 0.05 \,\text{W}\,\text{m}^{-1}\,\text{K}^{-1}$. In summary, this iterative fitting method allows for achieving good agreement with the theoretical model as well as the adequate goodness of fit ($>95\%$) and a minimum root mean squared error.

It may be stated that the independent determination of several thermal parameters in a single experiment became possible, as the measurements were performed for the varied thicknesses of the sample, which was equivalent to multiple experiments on the same system (Fig. S2 in the Supplemental Material [35]). Finally, for the justification, we also introduced these fitting parameters in our FEA model structure like the reference sample. We observed a negligible thermal gradient at a low thickness in contrast to that for higher thickness where the interface does not influence the heat spreading (Figs. 4(f) and S5 in the Supplemental Material [35]). Moreover, at higher thicknesses, the direction of heat flow is also found to be anisotropic, having a slightly larger contribution toward the in-plane direction.

We compared the quantitative results with some of the reported perovskites obtained through other conventional techniques (Table S1 in the Supplemental Material [35], which includes Refs [19–26,29,51,52]). We found that the obtained value of k_l having an ultralow nature matches well with other 2D perovskites, which is even lower than their 3D counterpart MAPbI$_3$ possessing a continuous inorganic framework of strong ionic/covalent bonds [19,20,28,29,53]. It is also found that the in-plane thermal conductivity of the

2D perovskite (PEA$_2$PbI$_4$) is larger than its one-dimensional counterpart (PEAPbI$_3$) [19]. On the other hand, $\Delta_{\text{anis}} = 3.39$ was also found to be larger than a recent report of a similar 2D perovskite (BA$_2$PbI$_4$) having a value of 1.5 [20]. It should be noted that most of the existing techniques to measure anisotropic thermal conductivity involve a different set of macroscopic experiments [19,20,25,26,54]. In this regard, our method of measuring anisotropic thermal conductivity using the xSThM method with a single set of measurements and nanoscale resolution paves the way as an alternative and efficient route.

3. Evaluation of the systematic error

As this technique is comparatively unique, to evaluate the size of the systematic error, these results were corroborated with similar measurements and analysis on a standard sample with known low thermal conductivity in the range of the 2D perovskite we studied (Fig. 5). We picked an isotropic polymer thin film SU-8 for such study, which is reported to possess a thermal conductivity of $0.2 \,\text{W}\,\text{m}^{-1}\,\text{K}^{-1}$ [55,56]. We repeated similar xSThM measurements and analytical fitting to quantify the thermal conductivity and anisotropy of the material so that the effect of any systematic error could be understood. In Fig. 5(a), the mapping of thermal voltages of the Si/SiO$_2$/SU-8 control sample has been presented along the wedge cut prepared from a similar BEXP method. We observed low thermal voltages at the Si region followed by a clear increase at the SiO$_2$ layer, inferring a decrease in thermal spreading due to a much higher thermal conductivity of Si than SiO$_2$. Similarly, in the SU-8 polymer layer, a further
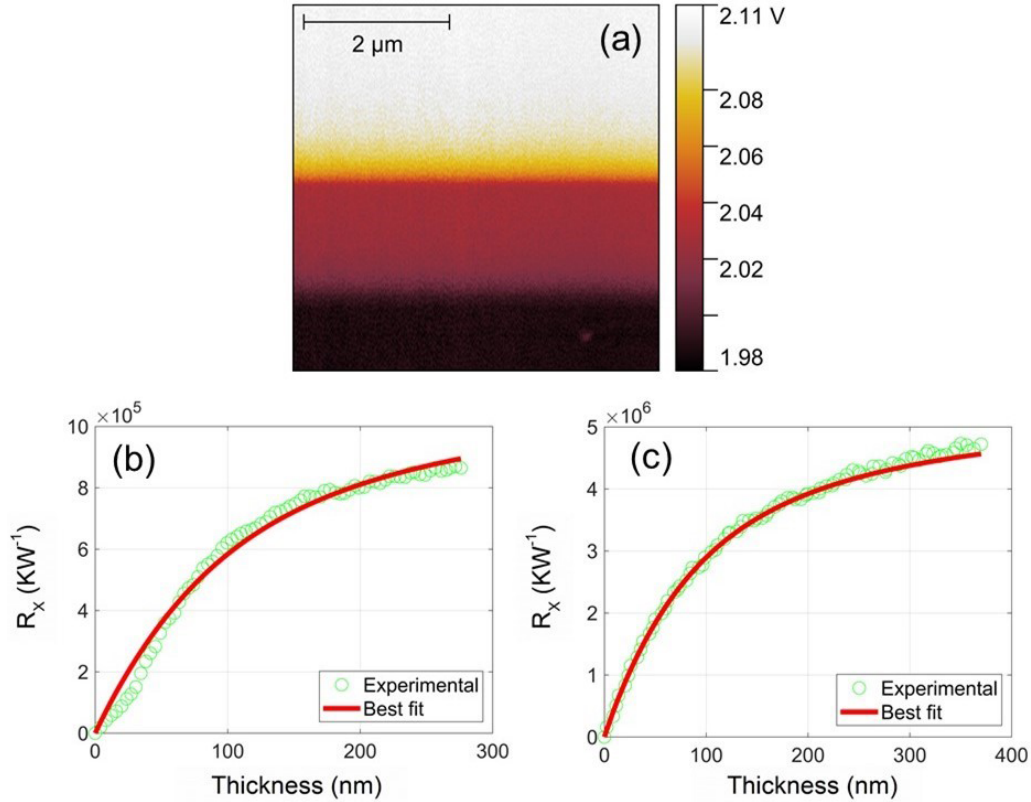
FIG. 5. (a) Thermal signal image of the $Si/SiO_2/SU-8$ heterojunction as obtained from cross-sectional scanning thermal microscopy (xSThM). (b) and (c) The fitting plots for Si/SiO_2 and $SiO_2/SU-8$ heterojunctions, respectively, through the analytical model.

increase in the thermal voltage was observed compared with SiO_2, indicating even smaller thermal conductivity. To quantify the average $k_{avg}(k_{l,\ anis})$ $k_{l,xy}$, $k_{l,z}$ of the SU-8 layer using our model, we similarly applied the two-step fitting. In the first step, the analytical fitting [Fig. 5(b)] returned the value of a and C_{corr} as fitting parameters. These served as inputs at the second step of fitting of SU-8 on the SiO_2 [Fig. 5(c)] heterostructure to obtain k_l ($k_{l,\ anis}$, $k_{l,xy}$, $k_{l,z}$). The results showed that $k_{avg}(k_{l,\ anis})$ of the top SU-8 layer lies close to $0.24 \pm 0.01 \, W \, m^{-1} \, K^{-1}$ with adequate goodness of fit; on the other hand, Δ_{anis} was found to be 0.92 ($k_{l,xy} = 0.23 \pm 0.01 \, W \, m^{-1} \, K^{-1}$ and $k_{l,z} = 0.25 \pm 0.01 \, W \, m^{-1} \, K^{-1}$), signifying the near isotropic nature of the thermal conductivity. Hence, we could claim the size of the systematic error through this unique xSThM approach in measuring the thermal conductivity as $\sim 20\%$ and $<10\%$ for the anisotropy factor, confirming that quantification of anisotropic thermal transport in 2D perovskite is highly reliable.

E. Origin of anisotropic thermal transport in 2D perovskite

In this paper, we reveal the occurrence of thermal anisotropy in this compound. Such anisotropy in thermal transport can be explained by considering the structural landscape of a general 2D-RP perovskite and associated phonon transport [Fig. 6(a)]. In such materials, the metal halide octahedra form infinite sheets in the in-plane direction, and the organic spacer molecules are located between two successive sheets in the out-of-plane direction. As mentioned

earlier, the large spacer cation (for example, PEA chains) is aligned in the out-of-plane direction having covalent bonds (C-C and C-N). In addition, weak van der Waals and electrostatic interactions can be found between two vertically stacked organic chains and at the organic-inorganic interfaces. On the other hand, there are strong ionic bonds in the in-plane direction originating from the continuous $[PbI_4]^{2-}$ octahedral framework [20,42,43,57]. It may be noted that the component of the thermal conductivity tensor can be expressed as

$$k_{l,\alpha\beta} = \sum_q C_v q \vartheta_{q,\alpha} \vartheta_{q,\beta} \tau_q, \tag{6}$$

where q indexes the phonon wave vector, $C_v q$ is the mode-wise heat capacity, $\vartheta_{q,\alpha}$ and $\vartheta_{q,\beta}$ are the mode-wise group velocity projected onto the α and β directions, respectively, and τ_q is the mode-wise lifetime. As such, C_v does not have any directional dependence in contrast to ϑ and τ in governing the anisotropic thermal transport in the compound. Along the in-plane direction, the presence of a continuous $[PbI_4]^{2-}$ octahedral framework allows uninterrupted pathways for heat transport [58]. In short, phonons would possess relatively large lifetimes and group velocities ($\vartheta_{q,xy}$) within these inorganic layers, resulting in a higher thermal conductivity ($k_{l,xy} = 0.45 \, W \, m^{-1} \, K^{-1}$). In contrast, the presence of organic-inorganic interfaces and the weak interactions of two vertically stacked organic chains would result in the scattering of phonons along the out-of-plane direction [57,59]. Hence,
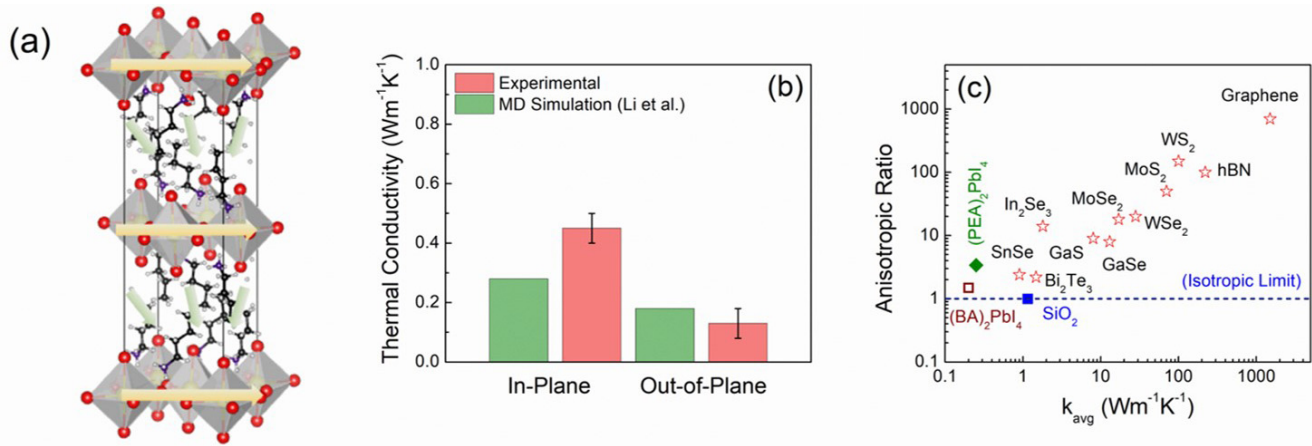
FIG. 6. (a) Heat (phonon) conduction pathways in a general two-dimensional (2D) Ruddlesden-Popper (RP) perovskite along in-plane and out-of-plane directions. (b) Comparison of in-plane and out-of-plane thermal conductivity of $(PEA)_2PbI_4$ with respect to molecular dynamics (MD) simulation of similar 2D perovskite [20]. (c) Anisotropic ratio vs average thermal conductivity of 2D-RP perovskite compared with other layered compounds in which the other data points were adapted [20].

thermal transport would be interrupted due to the shorter lifetime and group velocities ($\vartheta_{q,z}$) of phonons, leading to comparably lower thermal conductivity along the cross-plane ($k_{l,z} = 0.13\,\mathrm{W\,m^{-1}\,K^{-1}}$). In a nutshell, the anisotropy originates mainly due to the antagonism between continuous heat conduction in the inorganic layer along the plane vs the interrupted ones out of plane. Our experimental result matches well with the reports of Li *et al.* [20] as obtained from molecular dynamics (MD) simulations of a similar 2D perovskite [Fig. 6(b)]. However, the value of Δ_{anis} (~ 3.4) is found to be small compared with most of the other layered compounds [Fig. 6(c)] [60–65]; it may be noted that, due to the small volume fraction of the inorganic layers, the anisotropy becomes weak.

IV. CONCLUSIONS

In this paper, we measured thermal transport parameters ($k_{l,\mathrm{anis}}$, Δ_{anis} vis-à-vis $k_{l,xy}$, $k_{l,z}$) of an archetypal 2D perovskite system, namely, $(PEA)_2PbI_4$, through xSThM. The low-angle nanoscale quality wedge cut of the perovskite thin film on the SiO_2/Si substrate was obtained through the Ar-ion BEXP method that allowed us effectively in one SThM measurement to obtain thermal conductance data for the various thicknesses of all nanoscale layers. The experimentally obtained data were then used to first calibrate the SThM measurements and ultimately, with an analytical model validated by FEA simulation, to directly calculate the absolute values of in-plane and cross-plane anisotropic thermal conductivity $k_{l,xy}$ and $k_{l,z}$ of the 2D perovskite. We obtained an ultralow value of average thermal conductivity of this material of (k_{avg}) = $0.25 \pm 0.05\,\mathrm{W\,m^{-1}\,K^{-1}}$ for the 2D perovskite with an anisotropy factor ($k_{l,xy}/k_{l,z} \sim 3.4$) that we attribute to the unique structure of the perovskite, leading to different phonon lifetimes and phonon group velocities along cross-plane and in-plane directions. In this paper, we provide a technique to quantify the anisotropic thermal transport in 2D perovskites and provide physical insights that would be

useful for the thermal management of 2D perovskite-based optoelectronic devices and their potential applications in thermoelectric.

The data that support the findings of this paper are available from the corresponding author upon reasonable request.

[1] J. C. Blancon, H. Tsai, W. Nie, C. C. Stoumpos, L. Pedesseau, C. Katan, M. Kepenekian, C. M. M. Soe, K. Appavoo, M. Y. Sfeir *et al.*, Science **355**, 1288 (2017).

[2] L. T. Dou, A. B. Wong, Y. Yu, M. L. Lai, N. Kornienko, S. W. Eaton, A. Fu, C. G. Bischak, J. Ma, T. N. Ding *et al.*, Science **349**, 1518 (2015).

[3] C. R. Kagan, D. B. Mitzi, and C. D. Dimitrakopoulos, Science **286**, 945 (1999).

[4] C. M. M. Soe, C. C. Stoumpos, M. Kepenekian, B. Traore, H. Tsai, W. Y. Nie, B. H. Wang, C. Katan, R. Seshadri, A. D. Mohite *et al.*, J. Am. Chem. Soc. **139**, 16297 (2017).

[5] L. Etgar, Energy Environ. Sci. **11**, 234 (2018).

[6] S. Bellani, A. Bartolotta, A. Agresti, G. Calogero, G. Grancini, A. Di Carlo, E. Kymakis, and F. Bonaccorso, Chem. Soc. Rev. **50**, 11870 (2021).

[7] L. L. Mao, C. C. Stoumpos, and M. G. Kanatzidis, J. Am. Chem. Soc. **141**, 1171 (2019).

[8] B. K. Song, J. Hou, H. N. Wang, S. Sidhik, J. S. Miao, H. G. Gu, H. Q. Zhang, S. Y. Liu, Z. Fakhraai, J. Even *et al.*, ACS Mater. Lett. **3**, 148 (2021).

[9] L. N. Quan, Y. B. A. Zhao, F. P. G. de Arquer, R. Sabatini, G. Walters, O. Voznyy, R. Comin, Y. Y. Li, J. Z. Fan, H. R. Tan *et al.*, Nano Lett. **17**, 3701 (2017).

[10] X. Hong, T. Ishihara, and A. V. Nurmikko, Phys. Rev. B **45**, 6961 (1992).

[11] B. R. Wygant, A. Z. Ye, A. Dolocan, Q. Vu, D. M. Abbot, and C. B. Mullins, J. Am. Chem. Soc. **141**, 18170 (2019).

[12] Z. X. Gan, Y. C. Cheng, W. J. Chen, K. P. Loh, B. H. Jia, and X. M. Wen, Adv. Sci. **8**, 2001843 (2021).

[13] A. Burgos-Caminal, E. Socie, M. E. F. Bouduban, and J. E. Moser, J. Phys. Chem. Lett. **11**, 7692 (2020).

[14] F. T. Pei, N. X. Li, Y. H. Chen, X. X. Niu, Y. Zhang, Z. Y. Guo, Z. J. Huang, H. C. Zai, G. L. Liu, Y. M. Zhang *et al.*, ACS Energy Lett. **6**, 3029 (2021).

[15] S. N. Hsu, W. C. Zhao, Y. Gao, M. S. Akriti, X. F. Xu, B. W. Boudouris, and L. T. Dou, Nano Lett. **21**, 7839 (2021).

[16] S. J. Yang, D. Kim, J. Choi, S. H. Kim, K. Park, S. Ryu, and K. Cho, Adv. Mater. **33**, 2102797 (2021).

[17] X. G. Jia, J. Jiang, Y. Zhang, J. H. Qiu, S. B. Wang, Z. H. Chen, N. Y. Yuan, and J. N. Ding, Appl. Phys. Lett. **112**, 143903 (2018).

[18] A. D. Christodoulides, P. J. Guo, L. Y. Dai, J. M. Hoffman, X. T. Li, X. B. Zuo, D. Rosenmann, A. Brumberg, M. G. Kanatzidis, R. D. Schaller *et al.*, ACS Nano **15**, 4165 (2021).

[19] A. Giri, A. Z. Chen, A. Mattoni, K. Aryana, D. Zhang, X. Hu, S. H. Lee, J. J. Choi, and P. E. Hopkins, Nano Lett. **20**, 3331 (2020).

[20] C. Li, H. Ma, T. Y. Li, J. H. Dai, M. A. Rasel, A. Mattoni, A. Alatas, M. G. Thomas, Z. W. Rouse, A. Shragai *et al.*, Nano Lett. **21**, 3708 (2021).

[21] S. R. Li, Z. H. Dai, L. D. Li, N. P. Padture, and P. J. Guo, Rev. Sci. Instrum. **93**, 053003 (2022).

[22] A. Pisoni, J. Jacimovic, O. S. Barisic, M. Spina, R. Gaal, L. Forro, and E. Horvath, J. Phys. Chem. Lett. **5**, 2488 (2014).

[23] R. Heiderhoff, T. Haeger, N. Pourdavoud, T. Hu, M. Al-Khafaji, A. Mayer, Y. W. Chen, H. C. Scheer, and T. Riedl, J. Phys. Chem. C **121**, 28306 (2017).

[24] C. Shen, W. N. Du, Z. Y. Wu, J. Xing, S. T. Ha, Q. Y. Shang, W. G. Xu, Q. H. Xiong, X. F. Liu, and Q. Zhang, Nanoscale **9**, 8281 (2017).

[25] C. Pipitone, S. Boldrini, A. Ferrario, G. Garcia-Espejo, A. Guagliardi, N. Masciocchi, A. Martorana, and F. Giannici, Appl. Phys. Lett. **119**, 101104 (2021).

[26] M. A. Rasel, A. Giri, D. H. Olson, C. Y. Ni, P. E. Hopkins, and J. P. Feser, ACS Appl. Mater. Interfaces **12**, 53705 (2020).

[27] A. Makris, T. Haeger, R. Heiderhoff, and T. Riedl, RSC Adv. **6**, 94193 (2016).

[28] T. Haeger, M. Wilmes, R. Heiderhoff, and T. Riedl, J. Phys. Chem. Lett. **10**, 3019 (2019).

[29] T. Haeger, R. Heiderhoff, and T. Riedl, J. Mater. Chem. C **8**, 14289 (2020).

[30] S. Gomes, A. Assy, and P. O. Chapuis, Phys. Status Solidi A **212**, 477 (2015).

[31] A. J. Robson, I. Grishin, R. J. Young, A. M. Sanchez, O. V. Kolosov, and M. Hayne, ACS Appl. Mater. Interfaces **5**, 3241 (2013).

[32] Y. S. Muzychka, J. Thermophys. Heat Transf. **28**, 313 (2014).

[33] Y. S. Muzychka, M. M. Yovanovich, and J. R. Culham, J. Thermophys. Heat Transf. **18**, 45 (2004).

[34] J. Spiece, C. Evangeli, A. J. Robson, A. El Sachat, L. Haenel, M. I. Alonso, M. Garriga, B. J. Robinson, M. Oehme, J. Schulze *et al.*, Nanoscale **13**, 10829 (2021).

[35] See Supplemental Material at https://link.aps.org/supplemental/10.1103/PhysRevMaterials.7.023801 for further details including a note about the formation of the top Al layer during BEXP cut, schematic representation of the BEXP method with a cross-sectioned area of the material having different interfaces, SThM configuration, schematic view of the xSThM scanning along the cut sample with increasing thickness, dependence of thermal spreading resistance on different fitting parameters for the Si/SiO$_2$ heterostructure, comparison of simulation results on flat vs wedge geometry, multilayer geometry used for the FEA simulation of thermal transport and the thermal results for Si/SiO$_2$ and Si/SiO$_2$/2D perovskite heterojunctions, and a comparison table of thermal conductivities of different metal halide perovskites obtained through existing experimental techniques which includes Refs. [19–26,29,51,52].

[36] O. V. Kolosov, I. Grishin, and R. Jones, Nanotechnology **22**, 185702 (2011).

[37] D. Buckley, Z. R. Kudrynskyi, N. Balakrishnan, T. Vincent, D. Mazumder, E. Castanon, Z. D. Kovalyuk, O. Kolosov, O. Kazakova, A. Tzalenchuk *et al.*, Adv. Funct. Mater. **31**, 2008967 (2021).

[38] I. S. Bowen, Phys. Rev. **27**, 779 (1926).

[39] A. Assy and S. Gomes, Nanotechnology **26**, 355401 (2015).

[40] P. D. Tovee, M. E. Pumarol, M. C. Rosamond, R. Jones, M. C. Petty, D. A. Zeze, and O. V. Kolosov, Phys. Chem. Chem. Phys. **16**, 1174 (2014).

[41] P. D. Tovee and O. V. Kolosov, Nanotechnology **24**, 465706 (2013).

[42] G. B. Wu, R. Liang, Z. P. Zhang, M. Z. Ge, G. C. Xing, and G. X. Sun, Small **17**, 2103514 (2021).

[43] J. Yin, R. Naphade, L. G. Arzaluz, J. L. Bredas, O. M. Bakr, and O. F. Mohammed, ACS Energy Lett. **5**, 2149 (2020).

[44] X. Y. Gan, O. Wang, K. Y. Liu, X. J. Du, L. L. Guo, and H. X. Liu, Sol. Energy Mater. Sol. Cells **162**, 93 (2017).

[45] K. Z. Du, Q. Tu, X. Zhang, Q. W. Han, J. Liu, S. Zauscher, and D. B. Mitzi, Inorg. Chem. **56**, 9291 (2017).

[46] C. Evangeli, J. Spiece, S. Sangtarash, A. J. Molina-Mendoza, M. Mucientes, T. Mueller, C. Lambert, H. Sadeghi, and O. Kolosov, Adv. Electron. Mater. **5**, 1900331 (2019).

[47] J. Spiece, C. Evangeli, K. Lulla, A. Robson, B. Robinson, and O. Kolosov, J. Appl. Phys. **124**, 015101 (2018).

[48] T. Yamane, N. Nagai, S. Katayama, and M. Todoki, J. Appl. Phys. **91**, 9772 (2002).

[49] H. R. Shanks, P. H. Sidles, P. D. Maycock, and G. C. Danielson, Phys. Rev. **130**, 1743 (1963).

[50] F. R. Brotzen, P. J. Loos, and D. P. Brady, Thin Solid Films **207**, 197 (1992).

[51] X. Long, Z. Y. Pan, Z. L. Zhang, J. J. Urban, and H. Wang, Appl. Phys. Lett. **115**, 072104 (2019).

[52] T. Haeger, M. Ketterer, J. Bahr, N. Pourdavoud, M. Runkel, R. Heiderhoff, and T. Riedl, J. Phys. Mater. **3**, 024004 (2020).

[53] C. Y. Ge, M. Y. Hu, P. Wu, Q. Tan, Z. Z. Chen, Y. P. Wang, J. Shi, and J. Feng, J. Phys. Chem. C **122**, 15973 (2018).

[54] P. Q. Jiang, X. Qian, and R. G. Yang, Rev. Sci. Instrum. **89**, 094902 (2018).

[55] J. L. Lai, C. J. Liao, and G. D. Su, Sensors **12**, 16390 (2012).

[56] S. H. Oh, K.-C. Lee, J. Chun, M. Kim, and S. S. Lee, J. Micromech. Microeng. **11**, 221 (2001).

[57] P. J. Guo, C. C. Stoumpos, L. Mao, S. Sadasivam, J. B. Ketterson, P. Darancet, M. G. Kanatzidis, and R. D. Schaller, Nat. Commun. **9**, 2019 (2018).

[58] P. S. Cheng, N. Shulumba, and A. J. Minnich, Phys. Rev. B **100**, 094306 (2019).

[59] W. L. Ong, E. S. O'Brien, P. S. M. Dougherty, D. W. Paley, C. F. Higgs, A. J. H. McGaughey, J. A. Malen, and X. Roy, Nat. Mater. **16**, 83 (2017).

[60] P. Q. Jiang, X. Qian, R. G. Yang, and L. Lindsay, Phys. Rev. Mater. **2**, 064005 (2018).

[61] H. J. Jang, J. D. Wood, C. R. Ryder, M. C. Hersam, and D. G. Cahill, Adv. Mater. **27**, 8017 (2015).

[62] P. Q. Jiang, X. Qian, X. K. Gu, and R. G. Yang, Adv. Mater. **29**, 1701068 (2017).

[63] R. McKinney, P. Gorai, E. S. Toberer, and V. Stevanovic, Chem. Mat. **31**, 2048 (2019).

[64] C. L. Hsin, J. H. Huang, P. Spiewak, L. Ciupinski, and S. W. Lee, Appl. Surf. Sci. **494**, 867 (2019).

[65] J. S. Kang, H. Wu, M. Li, and Y. J. Hu, Nano Lett. **19**, 4941 (2019).